**G. I. Mahmood**
Graduate Student.

**M. L. Hill**
Graduate Student.

**D. L. Nelson**
Graduate Student.

**P. M. Ligrani**[1]
Professor.

Convective Heat Transfer Laboratory,
Department of Mechanical Engineering,
University of Utah,
Salt Lake City, UT 84112

**H.-K. Moon**
Consulting Engineer.

**B. Glezer**
Head, Turbine Cooling and Heat Transfer Analysis.

Solar Turbines, Inc.,
Turbine Cooling Design and Analysis,
San Diego, CA 92186

# Local Heat Transfer and Flow Structure on and Above a Dimpled Surface in a Channel

*Experimental results, measured on and above a dimpled test surface placed on one wall of a channel, are given for Reynolds numbers from 1250 to 61,500 and ratios of air inlet stagnation temperature to surface temperature ranging from 0.68 to 0.94. These include flow visualizations, surveys of time-averaged total pressure and streamwise velocity, and spatially resolved local Nusselt numbers, which are measured using infrared thermography, used in conjunction with energy balances, thermocouples, and in situ calibration procedures. The ratio of channel height to dimple print diameter is 0.5. Flow visualizations show vortical fluid and vortex pairs shed from the dimples, including a large upwash region and packets of fluid emanating from the central regions of each dimple, as well as vortex pairs and vortical fluid that form near dimple diagonals. These vortex structures augment local Nusselt numbers near the downstream rims of each dimple, both slightly within each depression, and especially on the flat surface just downstream of each dimple. Such augmentations are spread over larger surface areas and become more pronounced as the ratio of inlet stagnation temperature to local surface temperature decreases. As a result, local and spatially averaged heat transfer augmentations become larger as this temperature ratio decreases. This is due to the actions of vortical fluid in advecting cool fluid from the central parts of the channel to regions close to the hotter dimpled surface.*
[DOI: 10.1115/1.1333694]

## Introduction

To reduce or eliminate the need to employ film cooling, new attention has been devoted to internal cooling schemes for turbine airfoils. Internal schemes are advantageous in several respects, including smaller requirements for compressor air, and little or no aerodynamic penalties. However, the augmentation of surface heat transfer coefficients and the flow structural characteristics responsible for such augmentations must be understood for optimal internal passage design. The present investigation focuses on the use and effects of dimples in providing such augmentations. Such surface geometries have been long recognized to provide aerodynamic and flow benefits for a variety of applications [1]. Here, heat transfer and flow structure are investigated in a channel, with dimples on one surface, which models the passages used to cool turbine airfoils employed in gas turbine engines used for power generation.

Many early investigations of the effects of dimple cavities on heat transfer and flow structure are by Russian investigators. Much of this work focuses on flow and/or heat transfer either inside or downstream of single or multiple concave depressions on a wall in an internal passage. Of these studies, Gromov et al. [2] describe symmetric and nonsymmetric streamlines and flow patterns produced by such cavities with a variety of sizes. Cells of fluid motion are described in the form of tightening spirals, helical streamlines, and horse-shoe shaped vortices. Afanasyev et al. [3] describe the heat transfer enhancement mechanism for flows over walls indented with regular arrays of spherical pits. This includes the dynamic and thermal properties of the boundary layer on the smooth surface between the pits. Enhancements of 30-40 percent without appreciable pressure losses (compared to a smooth surface) are reported. Belen'kiy et al. [4] describe heat transfer intensification from a tube surface fitted with a staggered array of concave dimples on surfaces of annular internal passages. Results applicable to shell-and-tube heat exchangers show maximum relative increases in overall heat transfer for deep cavities of about 2.5, and for shallow cavities of about 2.0, compared with smooth annular internal passages. High pressure losses are also reported. Bearman and Harvey [5] investigate crossflows over dimpled cylindrical surfaces. The geometry of the dimples corresponds to the optimum concavity depth found by Kimura and Tsutahara [6] for minimum drag on cylinders. At high Reynolds numbers, significantly lower drag coefficients are present with arrays of dimples compared to smooth cylinders.

More recently, Kesarev and Kozlov [7] present distributions of local heat transfer coefficients inside a hemispherical cavity and indicate that the convective heat flux from the cavity is higher than that from the surface of a plane circle of the same diameter as the cavity diameter. The authors also describe the effects of turbulence intensity of the incident flow on the local heat flux and on the local shear stress on the cavity surface. Terekhov et al. [8] present experimental measurements of flow structure, pressure fields, and heat transfer in a channel also with a single dimple on one surface. Different magnitudes and frequencies of flow oscillations are described, along with heat transfer and pressure loss dependence on dimple geometry. From flow visualizations, Zhak [9] describes a variety of vortex structures in different shaped rectangular cavities. Schukin et al. [10] present results applicable to gas turbine cooling. Average heat transfer coefficients are reported from the measurements on a heated plate downstream of a single hemispherical cavity in a diffuser channel and in a convergent channel. The study provides data on the influences of the mainstream turbulence intensity level and the angles of divergence and convergence on heat transfer augmentation.

Other recent work by Chyu et al. [11] includes data on the influences of Reynolds number on local heat transfer coefficient distributions on surfaces imprinted with staggered arrays of two different shapes of concavities. Their measurements for $H/D$ of 0.5, 1.5, and 3.0 show distributions of heat transfer coefficients everywhere on the surfaces that are significantly higher than val-

[1]Corresponding author.

Contributed by the International Gas Turbine Institute and presented at the 45th International Gas Turbine and Aeroengine Congress and Exhibition, Munich, Germany, May 8–11, 2000. Manuscript received by the International Gas Turbine Institute February 2000. Paper No. 2000-GT-230. Review Chair: D. Ballal.

  

ues in channels with smooth walls. Over a range of Reynolds numbers, enhancement of the overall heat transfer rate is about 2.5 times smooth surface values, and pressure losses are about half the values produced by conventional rib turbulators. Lin et al. [12] present computational simulation results of the flow structures and resulting surface heat transfer distributions for the same geometries and flow conditions. Flow streamlines and temperature distributions are presented that provide insight into flow structural characteristics produced by the dimples. Another recent investigation by Gortyshov et al. [13] employs spherical dimples, called spherical intensifiers, placed at different relative positions on the two opposite surfaces of a narrow channel. Moon et al. [14] give data for $H/D$ from 0.37 to 1.49 that illustrate the effects of channel height on heat transfer and pressure losses on a surface with a staggered pattern of dimples. According to the investigators, improvements in heat transfer intensification and pressure losses remain at approximately constant levels over the ranges of Reynolds number and channel height investigated.

The present study is different from other investigations of the influences of dimples on flow and heat transfer because spatially resolved distributions of local Nusselt numbers, instantaneous flow structure (from flow visualizations), and distributions of total pressure and streamwise velocity are provided and interrelated to each other. Such data are presented for locations along the dimpled surface at different Reynolds numbers, and at different ratios of air inlet stagnation temperature to local surface temperature. Magnitudes of this temperature ratio include values in the range of application to gas turbine airfoil internal cooling passages. Particular attention is paid to the local flow characteristics that are responsible for augmentations of local Nusselt numbers.

## Experimental Apparatus and Procedures

**Channel and Test Surface for Heat Transfer Measurements.** A schematic of the facility used for heat transfer measurements is shown in Figs. 1($a$) and 1($b$). The air used within the facility is circulated in a closed loop. One of two circuits is employed, depending upon the Reynolds number and flow rate requirements in the test section. For Reynolds numbers $Re_H$ less than 20,000, a 102 mm pipe is connected to the intake of an ILG Industries 10P type centrifugal blower. For higher Reynolds numbers, a 203 mm pipe is employed with a New York Blower Co. 7.5 HP, size 1808 pressure blower. In each case, the air mass flow rate from the test section is measured (upstream of whichever blower is employed) using an ASME standard orifice plate and Validyne M10 digital pressure manometer. The blower then exits into a series of two plenums (0.9 m square and 0.75 m square). A Bonneville crossflow heat exchanger is located between two of these plenums, and is cooled with liquid nitrogen at a flow rate appropriate to give the desired air temperature at the exit of the heat exchanger. As the air exits the heat exchanger, it enters the second plenum, from which the air passes into a rectangular bell mouth inlet, followed by a honeycomb, two screens, and a two-dimensional 19.5:1 contraction ratio nozzle. Figure 1($b$) shows that this nozzle leads to a rectangular cross-sectional, 411 mm by 25.4 mm inlet duct, which is 1219 mm in length. This is equivalent to 25.4 hydraulic diameters (where hydraulic diameter is 47.8 mm). A trip is employed on the bottom surface of the inlet duct, just upstream of the test section, which follows with the same cross-sectional dimensions. It exits to a 0.60 m square plenum, which is followed by two pipes, each containing an orifice plate, mentioned earlier.

Figures 2($a$) and 2($b$) present the geometric details of the test surface, including dimple geometry. A total of 13 rows of dimples are employed in the streamwise direction, and 9 rows are employed in the spanwise direction in a staggered array. Also identified in Fig. 2($a$) is the test section coordinate system employed for the study. Note that the $Y$ coordinate is normal to the test surface.

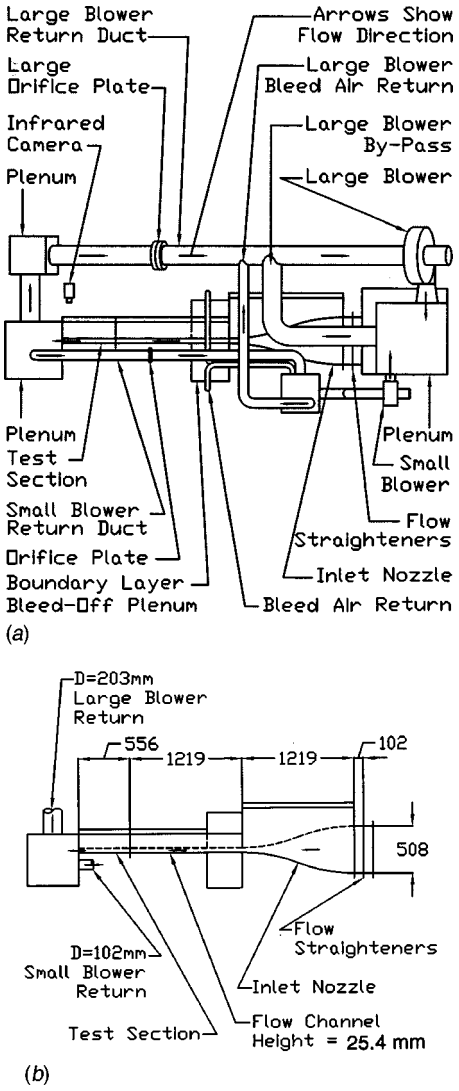


**Fig. 1 Schmeatic diagrams of ($a$) the experimental apparatus, and ($b$) a side view of the experimental apparatus with dimensions. All dimensions are given in mm.**

All exterior surfaces of the facility (between the heat exchanger and test section) are insulated with Styrofoam ($k$=0.024 W/mK), or two to three layers of 2.54-cm-thick, Elastomer Products black neoprene foam insulation ($k$=0.038 W/mK) to minimize heat losses. Calibrated copper-constantan thermocouples are located between the three layers of insulation located beneath the test section to determine conduction losses. Between the first layer and the 3.2-mm-thick acrylic, the dimpled test surface is a custom-made Electrofilm etched-foil heater (encapsulated between two thin layers of Kapton) to provide a constant heat flux boundary condition on the test surface. The acrylic surface contains 24 copper-constantan thermocouples, and is adjacent to the air stream. Each of these thermocouples is located 0.0508 cm just below this surface to provide measurements of local surface temperatures, after correction for thermal contact resistance and temperature drop through the 0.0508 cm thickness of acrylic. Acrylic is chosen because of its low thermal conductivity ($k$=0.16 W/mK at 20°C) to minimize streamwise and spanwise conduction along the test surface, and thus minimize ''smearing'' of spatially varying temperature gradients along the test surface. Acrylic also works well for infrared imaging because its surface emissivity ranges from 0.60 to 0.65. The power to the foil heater is controlled and regulated using a Variac power supply. Energy bal-

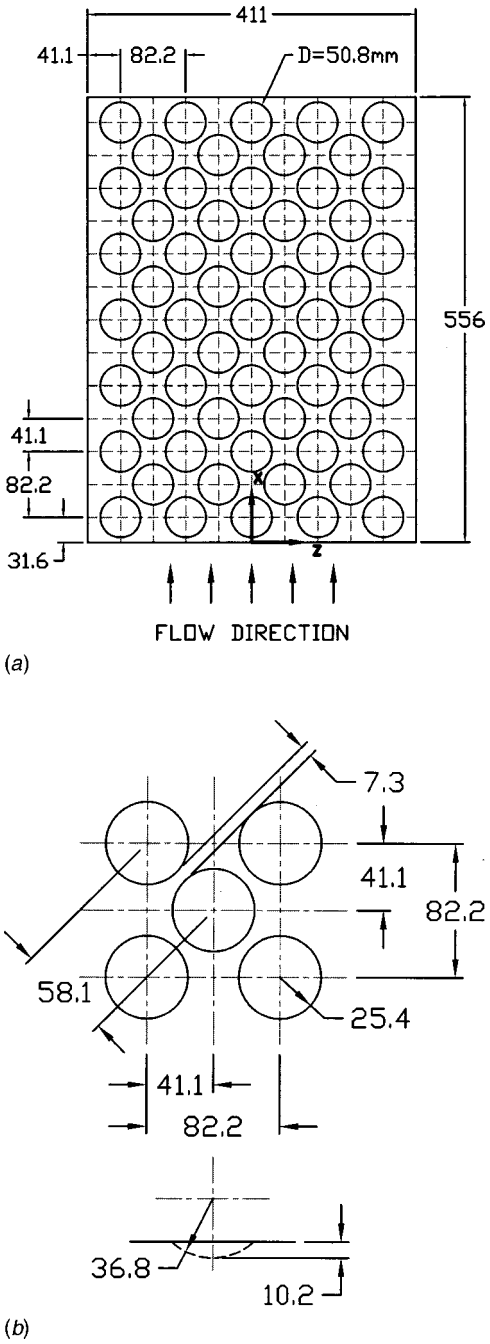


**Fig. 2 Schematic diagrams of: (*a*) the entire dimpled test surface, and (*b*) individual dimple geometry details. All dimensions are given in mm.**

ances, performed on the heated test surface, then allow determination of local magnitudes of the convective heat flux.

The mixed-mean temperature of the air entering the test section is measured using five calibrated copper-constantan thermocouples spread across its cross section. All measurements are obtained when the test facility at steady state, achieved when each of the temperatures from the 24 thermocouples (on the test surface) vary by less than 0.1°C over a 10 minute period.

**Local Nusselt Number Measurement**. To determine the surface heat flux (used to calculate heat transfer coefficients), the convective power provided by the etched foil heater is divided by the total area of the test surface (flat portions and dimples). Thus, local heat transfer coefficients and local Nusselt numbers can be considered to be based on the same area. This is a different approach than employed by Chyu et al. [11] and Moon et al. [14], who used a flat projected area to determine heat flux. As a result, heat transfer coefficients from those studies are about 16.4 percent higher than values from the present study when compared for the same geometry and flow conditions.

Spatially resolved temperature distributions along the dimpled test surface are determined using infrared imaging in conjunction with thermocouples, energy balances, digital image processing, and in situ calibration procedures. To accomplish this, the infrared radiation emitted by the heated interior surface of the channel is captured using a VideoTherm 340 Infrared Imaging Camera, which operates at infrared wavelengths from 8 $\mu$m to 14 $\mu$m. Temperatures, measured using the calibrated, copper-constantan thermocouples distributed along the test surface adjacent to the flow, are used to perform the in situ calibrations simultaneously as the radiation contours from surface temperature variations are recorded.

This is accomplished as the camera views the test surface through a custom-made, zinc-selenide window (which transmits infrared wave lengths between 6 and 17 $\mu$m) located on the top wall of the test section. Reflection and radiation from surrounding laboratory sources are minimized using an opaque shield, which covers the camera lens and the zinc selenide window. Frost build-up on the outside of the window is eliminated using a small heated air stream. The window is located just above the tenth to twelfth rows of dimples downstream from the leading edge of the test surface. Five to six thermocouple junction locations are usually present in the infrared field viewed by the camera. The exact spatial locations and pixel locations of these thermocouple junctions and the coordinates of a 12.7 cm by 12.7 cm field of view are known from calibration maps obtained prior to measurements. During this procedure, the camera is focused, and rigidly mounted and oriented relative to the test surface in the same way as when radiation contours are recorded.

With these data, gray scale values at pixel locations within videotaped images from the infrared imaging camera are readily converted to temperatures. Because such calibration data depend strongly on camera adjustment, the same brightness, contrast, and aperture camera settings are used to obtain the experimental data. The in situ calibration approach rigorously and accurately accounts for these variations.

Images from the infrared camera are recorded as 8-bit gray scale images on commercial videotape using a Panasonic AG-1960 video recorder. Images are then digitized using NIH Image vl.60 software, operated on a Power Macintosh 7500 PC computer. Subsequent software is used to convert each of 256 possible gray scale values to temperature at each pixel location using calibration data, and then determines values of local Nusselt numbers. Thermal conductivity in the Nusselt number is based on the average of the local wall temperature and the temperature of the air at the upstream inlet. Contour plots of local surface temperature and Nusselt number are prepared using DeltaGraph v4.0 software. Each individual image covers a 300 pixel by 300 pixel area. Hedlund and Ligrani [15] provide additional details on the infrared imaging and measurement procedures.

To check the repeatability and consistency of the results, infrared images from three different regions on the test surface (all located over the tenth, eleventh, and twelfth rows of dimples) are measured. Each of these regions covers the exact same area, which is the same as the center-to-center distance between four adjoining dimples in the tenth and twelfth rows. Results are identical for overlapping regions and repeatable well within uncertainty magnitudes when considered at similar locations with respect to different dimples. This indicates appropriate flow uniformity and periodicity in the test section, as well as correct test surface operation.

**Time-Averaged Total Pressure, Static Pressure, and Streamwise Mean Velocity.** A separate channel facility, with

interior geometry identical to that in the heat transfer facility, is employed for flow visualization as well as quantitative surveys of flow structure.

A United Sensor KAA-12 1/16-in.-dia miniature Kiel total pressure probe and a separate United sensor static pressure probe are used to obtain time-averaged surveys of total pressure and static pressure, respectively. These data are then used to deduce distributions of streamwise velocity. To obtain the surveys, the probe employed is mounted on an automated two-dimensional traverse, and inserted into the test section through a slot lined with foam to prevent air leakage. The output of the probe is connected either to a Validyne DP103-06 pressure transducer (which measures differential pressures up to 2.5 mm of water), or a Celesco LCVR pressure transducer (which measures differential pressures up to 20.0 mm of water). Signals from the transducer are then processed using a Celesco CD10D Carrier-Demodulator. Voltages from the Carrier-Demodulator are acquired using a Hewlett-Packard 44422A data acquisition card installed in a Hewlett-Packard 3497A data acquisition control unit. This control unit, the Superior Electric type M092-FD310 Mitas stepping motor on the two-dimensional traverse, a Superior Electric Modulynx Mitas type PMS085-C2AR controller, and a Superior Electric Modulynx Mitas type PMS085-D050 motor drive are controlled by a Hewlett-Packard A4190A Series computer. Contour plots of measured quantities are generated using a polynomial interpolating technique (within DeltaGraph software) between data points. In each survey plane, data points are spaced 2.54 mm apart.

*Flow Visualization.* Flow visualization using smoke is used to identify vortex structures and other secondary flow features. Smoke from two or three horizontally oriented smoke wires is employed for this purpose. These are located 3.2 mm, 6.4 mm, and 19.1 mm from the surface over the fifth row of dimples at $X=200-210$ mm. To accomplish this, each wire is first coated with Barts Pneumatics Corp. super smoke fluid and then powered using a Hewlett-Packard 6433B DC power supply. With this arrangement, the smoke forms into single thin lines parallel to the test surface. As the smoke is advected downstream, the secondary flows that accompany vortex and secondary flow development cause the smoke to be rearranged in patterns that show the locations and distributions of these flow phenomena. Smoke patterns are illuminated in different planes using thin sheets of light provided by a Colotran ellipsoidal No. 550, 1000 watt spotlight, and light slits machined in two parallel metal plates. Images are recorded using a Dage-MTI CCD72 camera and control box with a Computar Inc. 12.5 mm, F1.8 lens, connected to a Panasonic AG-1960 type four-head, multiplex video cassette recorder. Images recorded on video tape (taken individually or in sequence) are then digitized using a Sony DCR-TRV900 digital video camera recorder. The resulting images are then further processed using a Power Macintosh 7500 PC computer, and finally printed using a Panasonic PV-PD 2000 digital photo printer.

## Uncertainty Estimates

Uncertainty estimates are based on 95 percent confidence levels, and determined using procedures described by Moffat [16]. The uncertainty of temperatures measured with thermocouples is $\pm 0.15°C$. Spatial and temperature resolutions achieved with the infrared imaging are about 0.52 mm and 0.8°C, respectively. This magnitude of temperature resolution is due to uncertainty in determining the exact locations of thermocouples with respect to pixel values used for the *in situ* calibration. Local Nusselt number uncertainty is then about $\pm 6.8$ percent for $T_{0i}/T_w=0.68$. The corresponding Nusselt number ratio uncertainty is about $\pm 0.19$ (for a ratio of 2.00), or $\pm 9.6$ percent. Such $Nu/Nu_0$ uncertainties then increase as $T_{0i}/T_w$ becomes larger. Reynolds number uncertainty is about $\pm 1.7$ percent for $Re_H$ of 10,200. The uncertainties of total pressure (relative to atmospheric pressure), static pressure (relative to atmospheric pressure), and streamwise velocity are about $\pm 4.0$, $\pm 4.0$, and $\pm 2.5$ percent, respectively.

## Experimental Results and Discussion

**Baseline Nusselt Numbers.** Baseline Nusselt numbers are measured with a smooth test surface replacing the dimpled test surface at the same Reynolds numbers as employed in the dimpled channel. Other than the test surface, all geometric characteristics of the channel are the same as when a dimpled test surface is installed. These baseline values are used to normalize dimpled test surface values, and are thus used as a basis of comparison to dimpled test surface values. All baseline measurements are made with thermally and hydraulically fully developed channel flow, at a ratio of inlet stagnation temperature to wall temperature of 0.93-0.94.

**Spatially Resolved Nusselt Number Distribution.** Figure 3 presents spatially resolved Nusselt numbers measured on the dimpled test surface placed on one wall of the $H/D = 0.5$ channel. The opposite channel wall is smooth, as mentioned. Reynolds number $Re_H$ for the measurements is 10,200, and $T_{0i}/T_w=0.94$. Flow direction for the figure is from top to bottom in the direction of increasing *X/D*. The image shows dimples in the tenth to twelfth rows from the beginning of the test surface.

The locations of the circular concave depressions of the dimples correspond to circular $Nu/Nu_0$ contours in Fig. 3. Lower Nusselt number ratios are located over the upstream halves of the depressions. Local Nusselt number ratios are then higher in the downstream halves. The highest values are then located near the downstream rims of each dimple, both slightly within each depression, and on the flat surface just downstream of each dimple. Consistent with the results of Kesarev and Kozlov [7] and Schukin et al. [10], most local values in the concave cavities are higher than values measured a smooth channel at the same Reynolds number and temperature ratio.

Referring to the area over *Z/D* from $-0.3$ to $+0.3$, and over *X/D* from 9.1 to 9.7, the high $Nu/Nu_0$ region is spread over a region that is approximately parallel to the downstream edge of the dimple. Two fingers from this region then extend downwards in the positive *X/D* direction, which are located near the spanwise edges of adjoining dimples. These fingers continue to extend downward in the $+X/D$ direction until they connect with high $Nu/Nu_0$ regions located on the flat surfaces just downstream of the adjacent dimples. With this arrangement, regions of high $Nu/Nu_0$

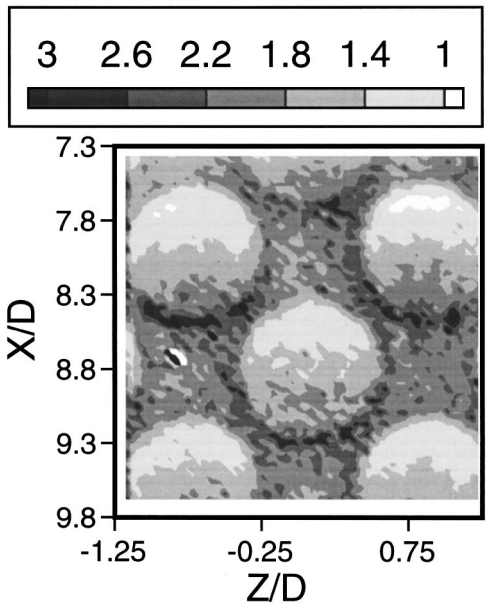


**Fig. 3 Local $Nu/Nu_0$ distributions measured at $Re_H=10.200$ and $T_{oi}/T_w=0.94$**

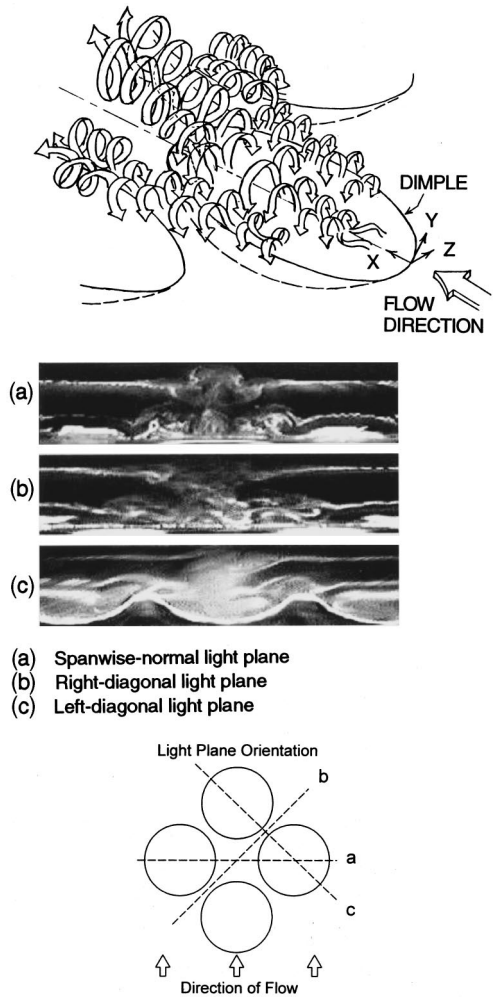


**Fig. 4 Sketch of three-dimensional flow structure and flow visualization images in different light planes at dimple row 10 for $Re_H$=1250 and $H/D$=0.5**

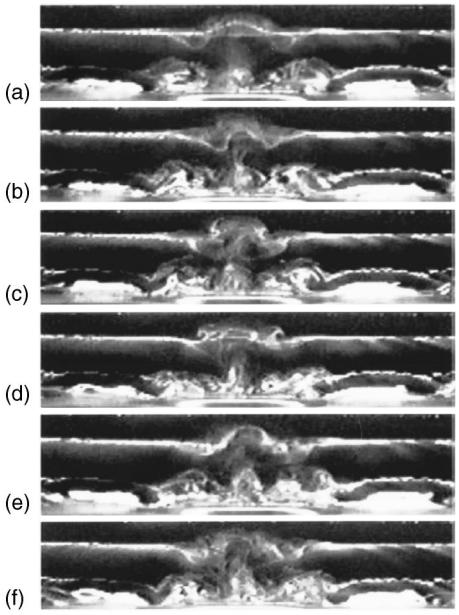


**Fig. 5 Time sequence of flow visualization images in the spanwise-normal light plane at dimple row 10 for $Re_H$=1250 and $H/D$=0.5: (*a*) $t$=0.0 s, $t^*$=0.0, (*b*) $t$=0.033 s, $t^*$=1.12, (*c*) $t$=0.067 s, $t^*$=2,27, (*d*) $t$=0.100 s, $t^*$=3.39, (*d*) $t$=0.133 s, $t^*$=4.50, (*f*) $t$=0.167 s, $t^*$=5.66**

are interconnected downstream of and to the sides of most dimples in the streamwise and spanwise adjacent rows.

**Instantaneous Flow Structure.** These regions of high local $Nu/Nu_0$ are the result of collections of vortex pairs and vortical fluid that is shed periodically from each dimple. The effects of this fluid on thermal transport are especially pronounced near downstream rims of dimples as well as on flat surfaces downstream of and between dimples, as mentioned. The outward shedding or ejection of fluid produces heat transfer augmentation from: (*i*) the periodicity and unsteadiness of the vortical fluid, and (*ii*) the strong secondary fluid motions of the vortical fluid and vortex pairs near the surface. A schematic drawing illustrating the character of this vortical fluid is shown in the top part of Fig. 4. Included in this figure are flow visualization images in three different planes with respect to the dimples: spanwise-normal, right-diagonal, and left-diagonal. The orientations of these planes are shown in the bottom portion of Fig. 4.

The shedding of fluid from the dimple is a key feature of the flow structure. The outward fluid motion from within the dimple (or upwash region) is present mainly at three locations with respect to each dimple. Each upwash region appears like the stem of a ''mushroom'' smoke pattern in spanwise-normal plane flow visualization images. The most prominent ''stem,'' corresponding to the strongest upwash, follows a streamwise-normal plane roughly down the centerline of each dimple. Such stems are apparent in: (*i*) streamwise views of smoke patterns illuminated in spanwise-normal planes (see Fig. 4). They are also occasionally apparent in: (*ii*) leftward-looking diagonal views of smoke patterns illuminated in right diagonal-normal planes, and (*iii*) rightward-looking diagonal views of smoke patterns illuminated in left diagonal-normal planes (again see Fig. 4). Two other stems and mushroom-shaped smoke patterns are located near the diagonal-spanwise edges of each dimple, or just downstream of these locations. Each upwash region stem leads to the ''petals'' of the ''mushroom'' located just above, at positions that are just at or just above the dimple horizon. Each ''petal'' corresponds to a vortex in the vortex pair. These vortex pairs are stretched as they are advected downstream (by the streamwise bulk flow above the dimple horizon), which causes them to become smaller in cross section and more elongated.

From a streamwise view looking downstream (spanwise-normal view in Fig. 4), the central upwash region and vortex pair are roughly symmetric with respect to a centerline-normal plane. From diagonal views (especially the right-diagonal plane in Fig. 4), the stem is elongated and bent in the downstream direction with the farthest downstream vortex elongated and somewhat distorted. This elongation is a result of viewing the vortex in a diagonal plane, and possibly a result of vortex stretching produced by the streamwise bulk flow above the dimple horizon. The axes of rotation, orientations, and structure of the vortices in these vortex pairs are about the same as they are shed from each dimple. That is, the vortices are always present temporarily at about the same locations during and after each shedding event.

At the diagonals of the dimple, the secondary flows in each vortex of each pair may impact on the flat surface adjacent to each dimple. As a result, additional smaller vortex pairs, collections of vortex pairs, or sometimes, short ''braids'' of vortical fluid are formed near dimple diagonals. This is illustrated in the schematic drawing at the top of Fig. 4, and is also apparent in the smoke patterns photographed in spanwise-normal and right- and left-diagonal planes. These pairs and packets of vortical fluid are then advected downstream as they are periodically impacted on the downstream rim of the dimpled edge and on the flat surface just downstream of the dimples. This vortical fluid is stretched further from the dimple edges (especially in dimple diagonal directions)

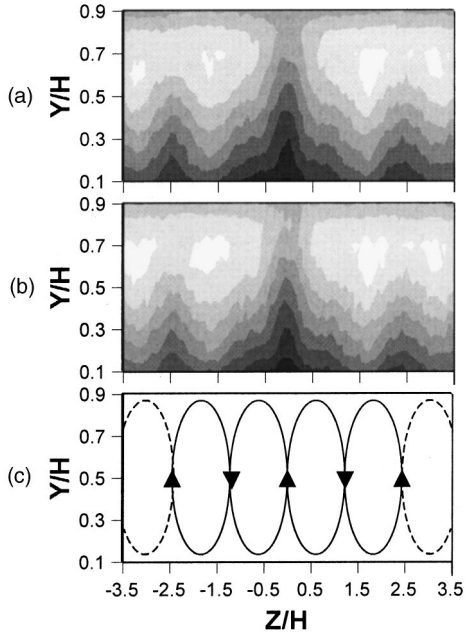


**Fig. 6 Surveys of time-averaged quantities in a spanwise-normal plane at $X/D$=11.88, which is located 53.2 mm downstream of the last row of dimples on the test surface for $Re_H$=9000:(*a*) total pressure ($P_a-\bar{P}_0$), adjacent contour lines are 2.0 Pa apart; (*b*) streamwise velocity $\bar{u}$, adjacent contour lines are 0.25 m/s apart; (*c*) schematic diagram of qualitative variations of large-scale, time-averaged secondary flow vectors**

as the Reynolds number increases. This causes the ''braids'' of vortical fluid to advect just above and into the dimple volumes which are located diagonal and adjacent to the dimple responsible for the initial upwash of fluid.

Another important feature of the flow structure produced by the dimpled surface is the periodicity associated with shedding of packets of vortical fluid from individual dimples. This results in a periodically varying flow structure above the dimple, which is illustrated by the time sequence of spanwise-normal flow visualization images in Fig. 5 (which are spaced 1/30 s apart from each other). Smoke patterns in the top parts of photographs (*a*), (*b*), (*e*), and (f) evidence secondary flows largely moving toward the dimple, whereas secondary flows largely move in the $+Y$ direction in the top parts of photographs (*c*) and (*d*). The small vortex pairs near dimple diagonals then oscillate to the left and right (as flow moves into and out of the side parts of the dimples) roughly in phase with the larger-scale motion. These events coincide with larger-scale inrush of flow to the dimple (photos (*a*) and (*b*) in Fig. 5), shedding of packets of vortical fluid from the dimple (photos (*c*) and (*d*)), and then another inrush event (photos (*e*) and (*f*)). This periodic sequence thus occurs continually such that the two types of events are not necessarily distinct or separate from each other. This means that some of the inward advection occurs as the shedding of fluid from the dimple is taking place, and vice versa.

Observations of videotaped flow visualization images show that the vortical fluid seems to be shed simultaneously with fluid shed from other dimples in the same spanwise row, but out of phase with the packets of fluid shed from dimples in an adjacent upstream or downstream dimple row. The inward advection and outward shedding must both take place (either simultaneously or alternatively) if continuity is to be satisfied for the flow near the dimpled surface.

**Time-Averaged Surveys of Total Pressure, Streamwise Velocity, and Secondary Flow Vectors.** Figure 6 presents data measured at $X/D$=11.88, which is a location about 53.2 mm downstream of the last row of dimples on the test surface. The data are time-averaged, and as such, illustrate flow characteristics which are different from, but complementary to, the flow visualization data. Each survey extends over the middle 80 percent of the height of the channel, and over $Z$ from $-1.75D$ to $+1.75D$ (or $-3.5H$ to $+3.5H$) on each side of the spanwise centerline of the test surface. The surveys are thus located just downstream of the centerline dimple in the 13th row as well as small portions of the dimples located on either side in the same streamwise row. The surveys are then also located just downstream of two other dimples, located in the twelfth row diagonally with respect to the dimples in the thirteenth row. The data in Fig. 6 are measured at a Reynolds number Re of 9000.

Apparent in the distributions of total pressure (part (*a*)) and streamwise velocity (part (*b*)) in Fig. 6 are important deficits near the dimpled surface. Each of these is shaped roughly like an inverted ''**V**'' and is located just downstream of a dimple cavity. Note that the deficits downstream of the dimples in the 13th row (at $Z/H$ of 0, for example) are larger and more pronounced than the deficits downstream of the dimples in the 12th row (at $Z/H$ of $+2.5$, $-2.5$). Each deficit results from upwash of packets of fluid away from dimples in the positive $Y$ direction.

Such upwash regions in the secondary flow field are shown schematically in part (*c*) of Fig. 6. These produce deficits in ($P_0$-$P$[overbar]$_0$) and $u$[overbar] by advecting relatively low-velocity/low total pressure fluid away from dimpled surfaces and away from the dimple horizon. Because of continuity and the boundary conditions imposed by the top and bottom walls of the channel, one downwash region is located between two adjacent upwash regions. As a result, Fig. 6(*c*) shows that two pairs of counterrotating secondary flow zones (or four total zones of rotating fluid) are present in the time-averaged flow field between the spanwise centerlines of two adjacent dimples in the same streamwise row. This is consistent with the upwash and downwash regions apparent in the flow visualization images in Figs. 4 and 5. However, upwash regions just above the dimples (where the flow visualization results are obtained) are more angled with respect to the dimple horizon at the dimple diagonals than the normally oriented upwash vectors shown in Fig. 6(*c*).

Because of the staggered arrangement of dimples in different streamwise rows, such time-averaged secondary flows are continually rearranged as flow advects over different streamwise rows of dimples. The downwash regions shown in Fig. 6(*c*) resulting from such activities advect fluid from the center portions of the channel to regions near $Y/D$=0. This and the resulting thinning of the shear layers near the dimpled surface aids the augmentation of

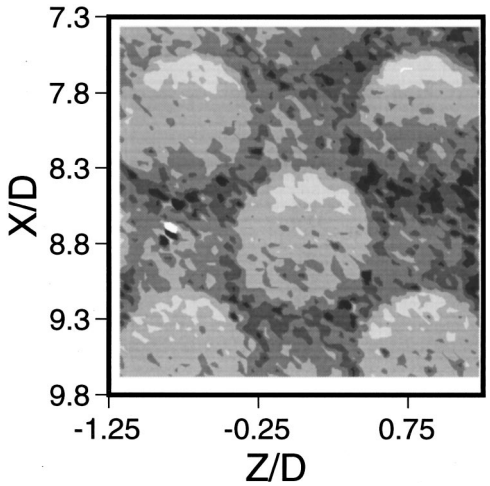


**Fig. 7 Local $Nu/Nu_0$ distributions measured at $Re_H$=61,500 and $T_{oi}/T_w$=0.92. Contour plot scale is given with Fig. 3.**

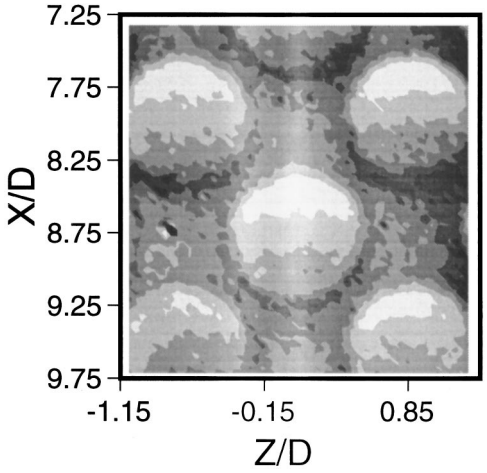


**Fig. 8 Local $Nu/Nu_0$ distributions measured at $Re_H$=13,300 and $T_{oi}/T_w$=0.83. Contour plot scale is given with Fig. 3.**

local Nusselt numbers, particularly the fingers of high $Nu/Nu_0$ in Fig. 3. As mentioned, these surface fingers extend downward in the positive *X/D* direction from the downstream edge of each dimple, and are located near the spanwise edges of adjoining dimples.

**Effects of Vortex Structures on Local Nusselt Numbers at Different Reynolds Numbers and Temperature Ratios.** Contour plots of local Nusselt number ratio distributions $Nu/Nu_0$ are presented in Figs. 7, 8, and 9. The data are presented for the same part of the test surface as employed to obtain the results in Fig. 3, but at different $Re_H$ or different $T_{0i}/T_w$ compared to the data in Fig. 3. Note that the $Nu/Nu_0$ scales in all four figures are the same.

Comparing the results in Fig. 7 for $Re_H$=61,500 and $T_{0i}/T_w$ =0.92 to the results in Fig. 3 for $Re_H$=10,200 and $T_{0i}/T_w$ =0.94 illustrates the influences of Reynolds number on local Nusselt number distributions. Qualitative and quantitative variations of $Nu/Nu_0$ are very similar in these two figures. Only slight differences are apparent in the bottom portions of the dimple cavities, where crescent-shaped contours of low magnitude are slightly larger at the lower Reynolds number. In contrast, on the flat parts of the surface, Nusselt number variations are a direct result of the three-dimensional unsteady secondary flows from the dimples. Here, the similarities of local $Nu/Nu_0$ variations in Figs. 3 and 7 evidence similar vortical and secondary flow structures at the different $Re_H$ investigated.

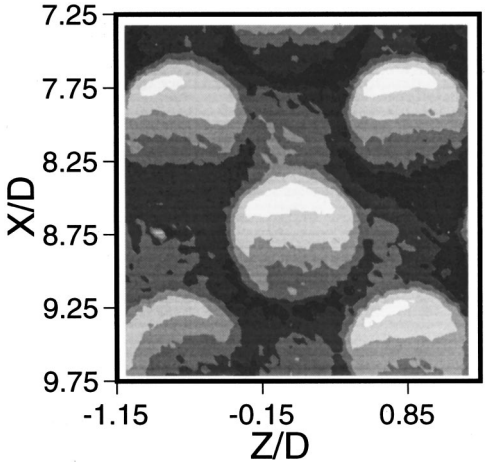


**Fig. 9 Local $Nu/Nu_0$ distributions measured at $Re_H$=12,800 and $T_{oi}/T_w$=0.68. Contour plot scale is given with Fig. 3.**

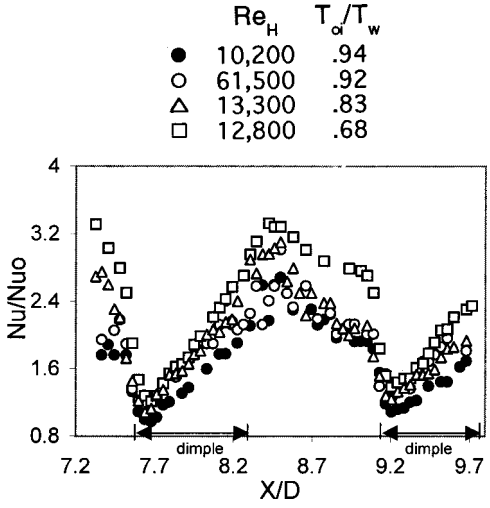


**Fig. 10 Local $Nu/Nu_0$ as dependent upon *X/D*, measured at different $Re_H$ and $T_{oi}/T_w$ at the eleventh row of dimples along a line of constant *Z/D* of 0.89**

The Nusselt number ratio distributions in Figs. 8 and 9 are for $T_{0i}/T_w$ of 0.83 and 0.68, respectively, compared to $T_{0i}/T_w$ =0.94 for Fig. 3. The Reynolds numbers for all three datasets range from 10,200 to 13,300, and thus, are all about the same. Comparing these three contour plots shows that as the ratio of inlet to wall temperature ratio decreases, the coolest part of the test surface, which corresponds to the highest values of $Nu/Nu_0$, intensifies, broadens, and extends farther away from the downstream rims of the dimples. This becomes more significant as the temperature ratio $T_{0i}/T_w$ decreases because vortex pairs and vortical fluid in the channel bring larger amounts of colder fluid from the central parts of the channel to regions near the dimpled surface. Larger-scale secondary flows, especially downwash regions, such as those evident in the time-averaged surveys of Fig. 6, also aid this process.

The effects of varying temperature ratio and Reynolds number are further illustrated by the results presented in Figs. 10 and 11. In each case, local $Nu/Nu_0$ values are given along one line along the test surface. For Fig. 10, variations with *X/D* are given along a line corresponding to *Z/D*=0.89. This corresponds approximately with the spanwise-centerline of a dimple in the eleventh row. In Fig. 11, $Nu/Nu_0$ data are presented as they vary with *Z/D*, along a line corresponding to *X/D*=8.46. This particular streamwise location is chosen because it corresponds with the largest variations of $Nu/Nu_0$ with *Z/D*. In each case, important increases of local Nusselt numbers are evident as the temperature ratio $T_{0i}/T_w$ decreases These are especially evident to the sides of the dimple at

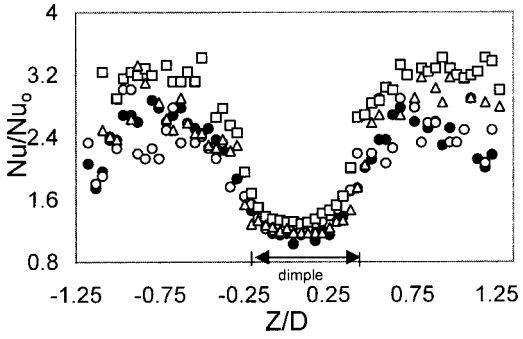


**Fig. 11 Local $Nu/Nu_0$ as dependent upon *Z/D*, measured at different $Re_H$ and $T_{oi}/T_w$ at the eleventh row of dimples along a line of constant *X/D* of 8.46. Symbols defined in Fig. 10.**

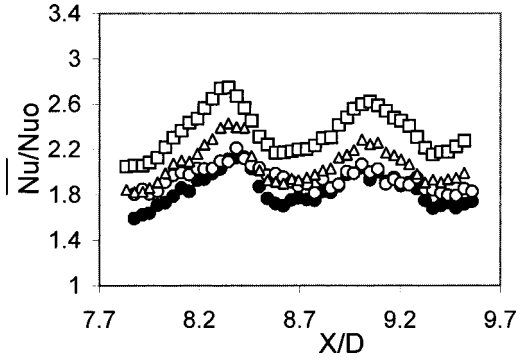


**Fig. 12 Spanwise-averaged $\overline{Nu}/Nu_0$ as dependent upon *X/D*, measured at different $Re_H$ and $T_{oi}/T_w$ at the eleventh and twelfth rows of dimples. Symbols defined in Fig. 10.**

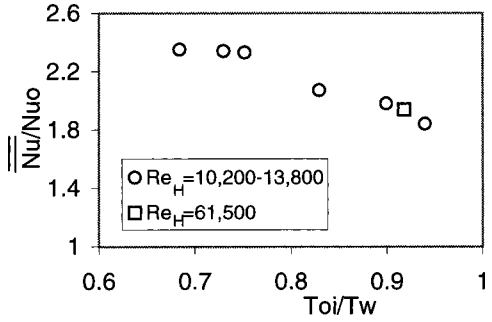


**Fig. 14 Globally averaged $\overline{\overline{Nu}}/Nu_0$ as dependent upon temperature ratio $T_{oi}/T_w$, measured at different $Re_H$ at the eleventh and twelfth rows of dimples**

*Z/D* from −1.0 to −0.5 and from +0.5 to +1.0 in Fig. 11, and downstream of a dimple in Fig. 10 at *X/D* from 8.2 to 9.0. Changes with Reynolds number are much less significant in these two figures, as expected. In each case, low Nusselt number ratios correspond with upstream portions of the dimple cavities, and the highest ratios are from locations near the rims or near the downstream edges of the dimples.

**Spatially Averaged Nusselt Number Behavior.** Spatially averaged Nusselt number data in Figs. 12, 13, and 14 further illustrate the influences of flow structure as the temperature ratio $T_{0i}/T_w$, and Reynolds number $Re_H$ are varied. In each case, spatial averages are obtained over a rectangular area from the center to center of adjacent dimples in the tenth and twelfth rows. This gives spatial averages representative of one complete period of dimple surface geometry.

Spanwise-averaged $\overline{Nu}/Nu_0$ versus *X/D* in Fig. 12, and streamwise-averaged $\overline{Nu}/Nu_0$ versus *Z/D* in Fig. 13 both show only small changes as Reynolds number increases from 10,200 to 61,500 and $T_{0i}/T_w$ is approximately constant. In contrast, $\overline{Nu}/Nu_0$ values increase significantly at each *X/D* or *Z/D* as temperature ratio decreases from 0.94 to 0.68 (and $Re_H$ is approximately constant). Such variations are consistent with local data, and provide further evidence of the important influences of the vortical fluid packets produced by the dimples. High local $\overline{Nu}/Nu_0$ values are thus mostly due to higher local values just downstream of and to the sides of the dimples, whereas troughs in $\overline{Nu}/Nu_0$ distributions are generally tied to low local Nusselt numbers within dimple cavities.

The globally averaged Nusselt number data in Fig. 14 are obtained by averaging local data in both the spanwise and streamwise directions. Only small changes with $Re_H$ are apparent. For constant $T_{0i}/T_w$, $\overline{\overline{Nu}}/Nu_0$ is proportional to $Re_H^{0.023}$. Such variations are qualitatively and quantitatively similar to ones measured by Chyu et al. [11] (after considering the different approaches for determination of heat transfer coefficients employed).

$\overline{\overline{Nu}}/Nu_0$ values shown in Fig. 14 increase by about 30 percent as the temperature ratio $T_{0i}/T_w$, decreases from 0.94 to 0.68 (and Reynolds number is approximately constant). This corresponds to a continual change of $\overline{\overline{Nu}}/Nu_0$ from 1.8 to about 2.4. Here, baseline Nusselt numbers $Nu_0$ (used for normalization) are measured at $T_{0i}/T_w = 0.93$-0.94.

According to Kays and Crawford [17], the variable property correction for such internal turbulent flows with wall heating and smooth (undimpled) surfaces is $(T_x/T_m)^{-0.5}$. This gives a decrease of variable-property, baseline $Nu_0$ of about 14 percent (compared to constant property values) as $T_{0i}/T_w$, decreases from 0.94 to 0.68. $Nu_0$ values determined using the Kays and Crawford [17] variable property correction can then be used to normalize dimple $\overline{\overline{Nu}}$ data at the same $T_{0i}/T_w$. With this approach, $\overline{\overline{Nu}}/Nu_0$ then ranges from 1.85 to about 2.89 as $T_{0i}/T_w$, decreases from 0.94 to 0.68.

Coolant passage friction factors are also important to designers of turbomachinery components. For $Re_H$ from 10,200 to 13,800, ratios of dimple surface friction factor to smooth surface friction factor are 1.51–1.55. Such values, along with heat transfer augmentations at the same Reynolds numbers, provide further evidence of the feasibility of dimpled passages for internal turbine airfoil cooling.

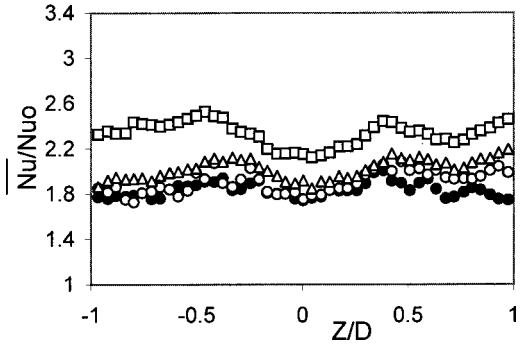


**Fig. 13 Streamwise-averaged $\overline{Nu}/Nu_0$ as dependent upon *Z/D*, measured at different $Re_H$ and $T_{oi}/T_w$ at the eleventh and twelfth rows of dimples. Symbols defined in Fig. 10.**

## Summary and Conclusions

Experimental results measured on and above a dimpled test surface placed on one wall of a channel are presented. Channel height *H* is 2.54 cm, and dimple print diameter *D* is 5.08 cm, giving $H/D = 0.5$. Flow structural characteristics and surface Nusselt numbers are given for Reynolds numbers $Re_H$ from 1250 to 61,500 and temperature ratios $T_{0i}/T_w$, ranging from 0.68 to 0.94. Flow visualizations show vortical fluid and vortex pairs shed from the dimples. These include a large upwash region and packets of fluid emanating from the central regions of each dimple, as well as vortex pairs and vortical fluid, which form near dimple diagonals. These help to augment surface heat transfer levels as they periodically impact the test surface and periodically produce an influx of bulk fluid. This occurs as the vortices and vortical fluid act to ''pump'' fluid to and away from the surface over different length scales, which helps to augment transport of different sized packets of fluid (with different temperatures) to and away from the surface. The periodic nature of the shedding of vortical fluid from the dimples also aids the heat transfer augmentation process.

The effects of the vortex structures are particularly pronounced near the downstream rims of each dimple, both slightly within

each depression, and on the flat surface just downstream of each dimple. The resulting high local Nusselt number region on the flat surface is spread over a region that is approximately parallel to the downstream edge of each dimple, and along two strips of flat surface located near the spanwise edges of downstream-diagonal, adjoining dimples.

Such augmentations are spread over larger surface areas and become more pronounced as the ratio of inlet stagnation temperature to local surface temperature decreases. This is due to the actions of different-sized vortex pairs and secondary flows in effectively advecting cool fluid from the central parts of the channel to regions close to the hotter dimpled surface. Downwash regions from the vortex pair emanating from the central part of each dimple, from the vortex pairs generated along dimple diagonals, and from rotating secondary flows spread over the entire channel cross section all make contributions to this process. As a result, local and spatially averaged heat transfer augmentations become larger as the $T_{0i}/T_w$, temperature ratio decreases.

## Acknowledgments

The work presented in this paper was performed as a part of the Advanced Turbine System Technology Development Project, sponsored both by the U.S. Department of Energy and Solar Turbines, Inc.

## Nomenclature

$D$ = dimple print diameter
$D_H$ = channel hydraulic diameter
$H$ = channel height
$h$ = heat transfer coefficient based on total surface area (dimples and flat) = $q''/(T_w - T_m)$
$k$ = thermal conductivity
Nu = Nusselt number = $hD_H/k$
$\mathrm{Nu}_0$ = baseline Nusselt number in a channel with smooth surfaces and no dimples
$P$ = pressure
$q''$ = surface heat flux
$\mathrm{Re}_H$ = Reynolds number based on channel height = $H\overline{U}/\nu$
$t$ = time
$t^*$ = normalized time = $t\overline{U}/H$
$T$ = temperature
$U$ = streamwise bulk velocity averaged over the channel cross section
$\overline{u}$ = time-averaged local streamwise velocity
$X$ = axial coordinate measured from test section inlet
$Y$ = normal coordinate measured from test section dimple horizon
$Z$ = spanwise coordinate measured from test section centerline
$\nu$ = kinematic viscosity
$\rho$ = density

### Subscripts

$a$ = ambient value
$i$ = time-averaged, test section inlet value
$m$ = time-averaged, local mixed-mean value
0 = total or stagnation value
$w$ = local wall value

### Superscripts

— = spanwise- or streamwise-averaged
= = globally averaged

## References

[1] Bearman, P. W., and Harvey J. K., 1976, ''Golf Ball Aerodynamics,'' Aeronautical Q., pp. 112–122.
[2] Gromov, P. R., Zobnin, A. B., Rabinovich, M. I., and Sushchik, M. M., 1986, ''Creation of Solitary Vortices in a Flow Around Shallow Spherical Depressions,'' Sov. Tech. Phys. Lett., **12**, No. 11, pp. 1323–1328.
[3] Afanasyev, V. N., Chudnovsky, Y. P., Leontiev, A. I., and Roganov, P. S., 1993, ''Turbulent Flow Friction and Heat Transfer Characteristics for Spherical Cavities on a Flat Plate,'' Exp. Therm. Fluid Sci., **7**, pp. 1–8.
[4] Belen'kiy, M. Y., Gotovskiy, M. A., Lekakh, B. M., Fokin, B. S., and Dolgushin, K. S., 1994, ''Heat Transfer Augmentation Using Surfaces Formed by a System of Spherical Cavities,'' Heat Transfer-Sov. Res., **25**, No. 2, pp. 196–203.
[5] Bearman, P. W., and Harvey, J. K., 1993, ''Control of Circular Cylinder Flow by the Use of Dimples,'' AIAA J., **31**, No. 10, pp. 1753–1756.
[6] Kimura, T., and Tsutahara, M., 1991, ''Fluid Dynamic Effects of Grooves on Circular Cylinder Surface,'' AIAA J., **29**, No. 12, pp. 2062–2068.
[7] Kesarev, V. S., and Kozlov, A. P., 1994, ''Convective Heat Transfer in Turbulized Flow Past a Hemispherical Cavity,'' Heat Transfer-Sov. Res., **25**, No. 2, pp. 156–160.
[8] Terekhov, V. I., Kalinina, S. V., and Mshvidobadze, Y. M., 1995, ''Flow Structure and Heat Transfer on a Surface With a Unit Hole Depression,'' Russ. J. Eng. Thermophys., **5**, pp. 11–33.
[9] Zhak, V. D., 1995, ''The Taylor–Goertler Vortices and Three-Dimensional Flow Evolution in Cavity,'' Russ. J. Eng. Thermophys., **5**, pp. 165–176.
[10] Schukin, A. V., Koslov, A. P., and Agachev, R. S., 1995, ''Study and Application of Hemispherical Cavities for Surface Heat Transfer Augmentation,'' ASME Paper No. 95-GT-59.
[11] Chyu, M. K., Yu, Y., Ding, H., Downs, J. P., and Soechting, F. O., 1997, ''Concavity Enhanced Heat Transfer in an Internal Cooling Passage,'' ASME Paper No. 97-GT-437.
[12] Lin, Y.-L., Shih, T. I.-P., and Chyu, M. K., 1999, ''Computations of Flow and Heat Transfer in a Channel With Rows of Hemispherical Cavities,'' ASME Paper No. 99-GT-263.
[13] Gortyshov, Y. F., Popov, I. A., Amirkhanov, R. D., and Gulitsky, K. E., 1998, ''Studies of Hydrodynamics and Heat Exchange in Channels With Various Types of Intensifiers,'' Proc. 11th International Heat Transfer Congress, **6**, pp. 83–88.
[14] Moon, H. K., O'Connell, T., and Glezer, B., 2000, ''Channel Height Effect on Heat Transfer and Friction in a Dimpled Passage,'' ASME J. Eng. Gas Turbines Power, **122**, pp. 307–313.
[15] Hedlund, C. R., and Ligrani, P. M., 1999, ''Local Swirl Chamber Heat Transfer and Flow Structure at Different Reynolds Numbers,'' ASME J. Turbomach., **122**, pp. 375–385.
[16] Moffat, R. J., 1988, ''Describing the Uncertainties in Experimental Results,'' Exp. Therm. Fluid Sci., **1**, No. 1, pp. 3–17.
[17] Kays, W. M., and Crawford, M. E., 1993, *Convective Heat and Mass Transfer*, McGraw-Hill, New York.